Supporting information (SI)

Fluidized-Bed Homogeneous Crystallization Recovery of High-Purity Lithium Phosphate from Industrial Wastewater

Van-Giang Le[1,], Ai-Quynh Nguyen[1], Phu Dong Le[2], Gia-Cuong Nguyen [1], Chi Thanh Vu[3]*

[1] Central Institute for Natural Resources and Environmental Studies, Vietnam National University, Hanoi 100000, Viet Nam.

[2] Faculty of Science & Food Technology, Lac Hong University, Viet Nam.

[3] 4EarthTech, Berkeley, CA 94704, United States.

* Corresponding author: levangiangcres@vnu.edu.vn

Table S1. Elemental concentrations of the raw lithium-containing wastewater

	Unit	Values
pH	-	8.51
Lithium	mg/L	2,174
Iron	mg/L	0.266
Aluminum	mg/L	0.228
Silicon	mg/L	1.672
Sodium	mg/L	291
Potassium	mg/L	17.48
Boron	mg/L	1.368
Calcium	mg/L	0.266
Sulfur	mg/L	2,395

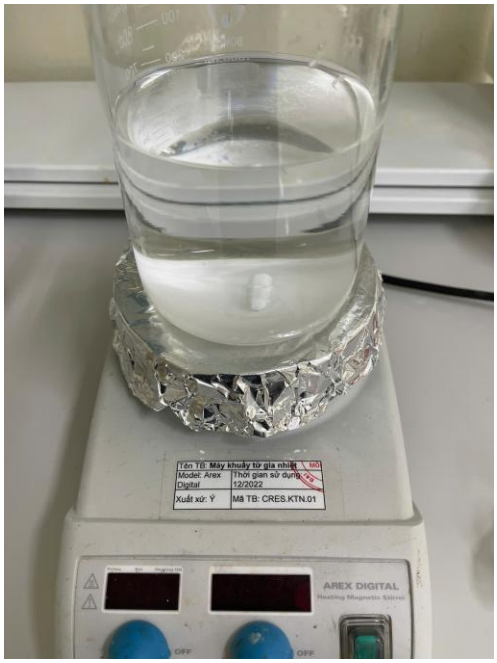

Figure S1. Jar-test setup for preparation of the homogeneous lithium phosphate particles (at an initial lithium concentration $[Li]_0$ of 2000 mg/L, sodium phosphate (Na_3PO_4) was subsequently added at a molar ratio $[Li^+]_0/[PO_4^{3-}]_0$ 1.2; the reaction was conducted at pH 11, temperature 50°C, and stirring speed 100 rpm for a duration of 4 hours in a 2000 mL beaker).

Text S1

Sampling and calculation of recovery/crystallization efficiencies and precipitation product's purity

Each sampling contained two samples collected from the top of the reactor at the reflux point (5 cm below the outlet). The difference of the two samples is displayed by the error bars in all concentration line graphs. Samples were filtered through a 0.45 μm filter for chemical analysis. Total recovery/removal (TR) quantifies the total lithium amount that was removed as precipitates.

$$\mathrm{TR}\ (\%) = \left(1 - \frac{[\mathrm{E}]_s \times \mathrm{Q_T}}{[\mathrm{E}]_0 \times \mathrm{Q_0}}\right) \times 100 \qquad \text{(S1)}$$

The crystallization ratio (CR) was evaluated from the unfiltered sample, referring to the removal of lithium in the form of fluidized pellets.

$$\mathrm{CR}\ (\%) = \left(1 - \frac{[\mathrm{E}]_T \times \mathrm{Q_T}}{[\mathrm{E}]_0 \times \mathrm{Q_0}}\right) \times 100 \qquad \text{(S2)}$$

Here, $[\mathrm{E}]_s$ (mg/L), $[\mathrm{E}]_T$ (mg/L), and $[\mathrm{E}]_0$ (mg/L) denote the effluent soluble, the effluent total concentration (including soluble and insoluble forms), and the inlet concentration, respectively. $\mathrm{Q_0}$ and $\mathrm{Q_T}$ refer to the volume (L) at the initial and time t, respectively.

After collection, the precipitates were dried at 45 ± 1 °C for 48 h. The mass fraction of lithium and phosphate in the crystals was analyzed from the digested solution (0.5 g precipitate was dissolved in 15 mL of 35% HCl solution, which was then diluted with DI water to a total volume of 100 mL).

$$\%\ \text{mass fraction} = \frac{\mathrm{C_D} \times V}{m} \times 100\% \qquad \text{(S3)}$$

where m (g), V (L), and C_D (g/L) represent the initial weight (0.1 g), the digested solution volume (15×10^{-3} L), and the measured concentrations of the digested solution, respectively.

Assuming lithium precipitates only as lithium phosphate, the mass purity of Li_3PO_4 can be determined as follows.

$$\mathrm{Li_3PO_4}\ \text{purity}\ (\%) = \frac{\%\ \text{mass fraction of Li}}{6.94} \times 115.79 \qquad \text{(S4)}$$

where 115.79 and 6.94 are the molecular masses of Li_3PO_4 and lithium, respectively.

Text S2

Material characterization of the product pellets

Surface morphology and elemental composition were examined using scanning electron microscopy coupled with energy-dispersive X-ray spectroscopy (SEM–EDS, Tabletop Microscopes TM4000Plus II, Hitachi). Due to the limitations of conventional EDS detectors in detecting lithium ions, the elemental presence of phosphorus and oxygen was used as indirect confirmation of Li_3PO_4 formation. Surface functional groups were identified via Fourier-transform infrared spectroscopy (FTIR, Thermo Fisher Scientific Nicolet 6700, Waltham, MA, USA) using a wavelength range of 400 – 4000 cm^{-1} at ambient temperature. Prior to analysis, samples were finely ground and embedded in KBr pellets to enhance IR transparency and signal resolution. Crystallographic structure and phase composition were investigated using X-ray diffraction (XRD, DX III, Rigaku Co., Ltd, Tokyo, Japan) within the 2θ range of 10° – 90° (scan rate 10°/min). The resulting diffraction spectra were processed using Jade 6 software, where peak fitting was performed to distinguish between crystalline and amorphous components. The degree of crystallinity was subsequently calculated based on the fitted profiles. Raman spectroscopy (HORIBA HR Evolution), which allows for phase verification and identification of possible structural disorder or secondary phosphate phases, was employed to further confirm the presence of Li_3PO_4 (wavelength range 100 – 4000 cm^{-1}).

Text S3

Effects of upflow velocity on FBHC performance

Upflow velocity (U) plays a pivotal role in regulating both crystallization kinetics and fluidization dynamics in an FBHC system. As shown in **Figure S2**, the TR and CR of lithium and phosphate were significantly influenced by variations of the upflow velocity. When the upflow velocity increased from 15 to 33 m/h, the TR of lithium and phosphate improved from 74.14% and 42.03% to 85.15% and 47.22%, respectively. During the same interval, the CR of lithium and phosphate shifted from 63.11% and 38.02% to 83.21% and 44.18%, respectively. This enhancement can be attributed to improved bed expansion and mixing conditions, which facilitate greater collision frequency between suspended nuclei and seed surfaces. The increased turbulence and better fluidization at moderate velocities enhance mass transfer, promote agglomeration of fine nuclei, and stabilize crystal growth on existing Li_3PO_4 particles.

However, as the upflow velocity further increased to 70 m/h, both TR and CR of lithium and phosphate increased slightly. Specifically, Li^+-TR improved from 85.16% to 90.51% and Li^+-CR rose slightly from 83.13% to 84.18%, while PO_4^{3-}-TR and PO_4^{3-}-CR increased to 52.22% and 49.86%, respectively. These slight increases can be attributed to excessive turbulence and overexpansion of the bed, which destabilize the fluidized particles and promote the elutriation of small nuclei before they can grow or agglomerate. Furthermore, high shear rates at elevated upflow velocities may induce crystal attrition, fragmentation, or even hinder retention time, thereby limiting the transformation of metastable flocs into well-structured granules. Taken together, moderate upflow velocities (25–35 m/h) are optimal for achieving high lithium and phosphate recovery, while ensuring favorable particle morphology and minimizing fines production.

We performed a more insightful study on the effects of upflow velocities (U) on the sizes of the formed pellets. **Figure S3** illustrates the particle size distribution of FBHC-formed pellets across different upflow velocities. From 15 to 30 m/h, the particle population was dominated by the 0.25 – 0.50 mm fraction, with a relatively small proportion below 0.25 mm, indicating that moderate hydrodynamic energy favored the formation of medium-sized granules. As U increased to 50 and to 70 m/h, the size distribution shifted toward smaller fractions, with a rising percentage of particles below 0.25 mm and a reduced proportion of pellets exceeding 0.42 mm, suggesting that excessive turbulence and overexpansion of the bed hindered sustained crystal growth and

promoted fines generation. The average pellet size decreased from ~0.45 mm at 30 m/h to ~0.3 mm at 70 m/h, confirming the negative impact of high U on stable granule formation.

From a theoretical standpoint, these behaviors are consistent with the hydrodynamic principles governing fluidized beds. According to the Ergun equation, fluidization initiates when the upward drag force equals the gravitational force acting on the particles. For low Reynolds numbers (Re < 10), the minimum fluidization velocity (U_{mf}) can be estimated using Eq. (S5):

$$U_{mf} = \frac{\Phi^2 \times D^2 \times \varepsilon_{mf}^3 \times (\rho_s - \rho_f) \times G}{150 \mu_f (1 - \varepsilon_{mf})} \quad \text{(S5)}$$

Substituting the physical properties of Li_3PO_4 (ρ_s = 1.864 g/cm³, D ≈ 0.045 cm, Φ ≈ 0.50), water (ρ_f = 0.9999 g/cm³, μ_f = 0.00894 g/cm·s), and void fraction (ε_{mf} ≈ 0.51), we got U_{mf} ≈ 13 – 15 m/h, which aligns well with the onset of effective fluidization observed in the experimental data. To ensure stable operation, the upflow velocity must exceed U_{mf} by 1.5–2 times, which corresponds to the optimal range of 25 – 35 m/h. Within this range, fluidization is sufficient to prevent channeling while avoiding excessive entrainment or turbulence.

In practice, these findings are further supported by long term operation data. We ran an extended FBHC experiment of 200 h, and the formed pellets had a mass median diameter of 0.20 mm and particle sizes ranged from 0.125–1.41 mm. These results confirm the robustness of FBHC in producing stable, recoverable Li_3PO_4 pellets under controlled hydrodynamic conditions.

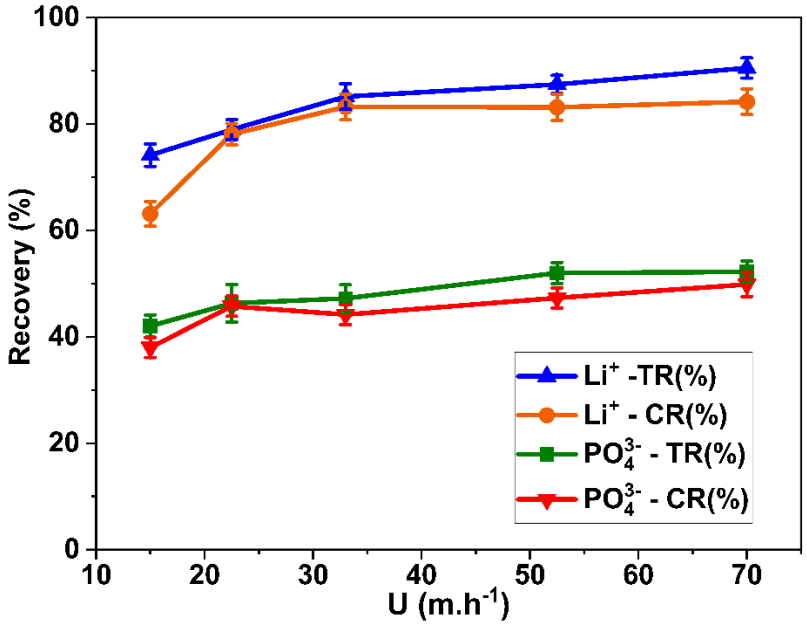

Figure S2. Effects of upflow velocity (experimental conditions: $[Li^+]_0$ of 1050 mg/L, pH_e of 11.5, L of 1.2 kg/m^2.h, T of 65 ºC, $[PO_4^{3-}]_0/[Li^+]_0$ of 0.5, bed height of 25 cm, and HRT of 23 min).

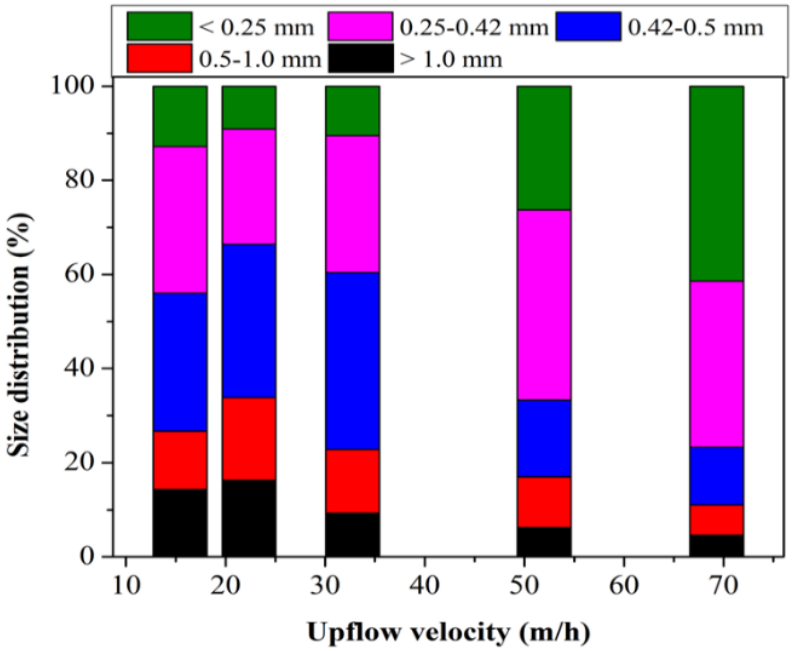

Figure S3. Effects of upflow velocity on particle size distribution of formed pellets (experimental conditions: $[Li^+]_0$ of 1050 mg/L, pH_e of 11.5, L of 1.2 kg/m^2.h, T of 65 ºC, $[PO_4^{3-}]_0/[Li^+]_0$ of 0.5, bed height of 25 cm, and HRT of 23 min).

Text S4

Effects of numbers of hydraulic retention time (HRT) on FBHC performance

Figure S4 illustrates the effects of numbers of HRT on the recovery efficiencies of Li^+ and PO_4^{3-} in the FBHC system. For both ions, recovery performance improved rapidly within the first few HRT cycles, indicating the quick establishment of favorable crystallization conditions. Li^+ exhibited consistently higher removal efficiencies compared to PO_4^{3-}, with values stabilizing at 84.55% for the CR mode and approximately 91% for the TR mode after 3 HRTs (~23 mins = time to reach equilibrium). In contrast, PO_4^{3-} removal stabilized at lower levels, around 73.55% in TR and 69.03% in CR, likely reflecting its more complex precipitation dynamics and possible mass transfer limitations. The relatively stable trends beyond 3 HRTs suggest that the FBHC system reached a quasi-steady-state operation, where nucleation and crystal growth were balanced with particle washout. These results confirm that extended HRT beyond 3 cycles offers limited additional improvement, highlighting the importance of optimizing HRT to balance performance and operational efficiency.

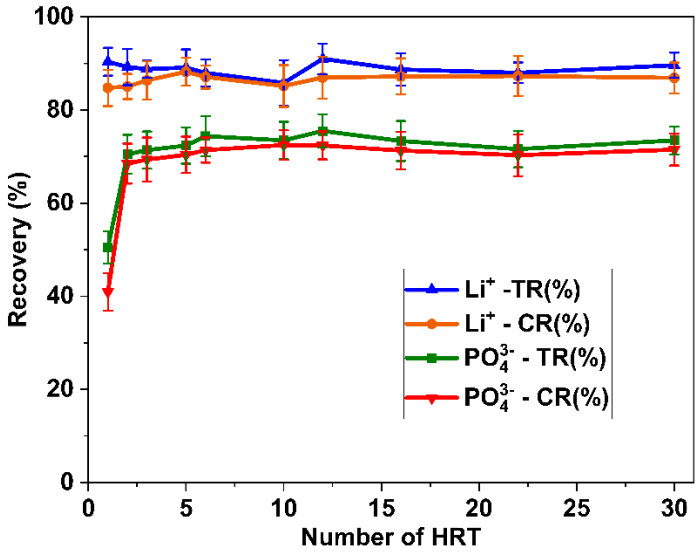

Figure S4. Effects of numbers of HRT (experimental conditions: $[Li^+]_0$ of 1050 mg/L, pH_e of 11.5, L of 1.2 kg/m^2.h, T of 65 ^{o}C, $[PO_4^{3-}]_0/[Li^+]_0$ of 0.5, bed height of 25 cm, and U of 15.3 m/h).

Text S5

Effects of initial lithium concentrations ($[Li^+]_0$) on the crystallinity and morphology of the product pellets

XRD patterns of Li_3PO_4 crystals synthesized at varying $[Li^+]_0$ (**Figure S5a**) consistently matched the standard diffraction pattern (JCPDS No. 15-0760) [1], confirming the formation of highly crystalline Li_3PO_4 with no detectable impurity phases. Notably, the diffraction peaks became broader and less intense with increasing $[Li^+]_0$, implying reduced crystallite phase (crystallite dimensions, calculated using the Scherrer equation, decreased from 40.4 nm at 1000 mg/L to 10.1 nm at 2500 mg/L). This inverse correlation suggests that elevated lithium concentrations favor rapid nucleation over subsequent crystal growth, leading to smaller crystallites with higher surface area. The FTIR spectrum (**Figure S5b**) exhibited a sharp peak around 1003.77 cm^{-1} as a result from the crystalline bonding between the metal ions and the phosphate group (the Li−P bond) [2]. This peak also showed a clear trend of becoming broader and less intense with increasing $[Li^+]_0$. The bending vibration of PO_4^{3-} was found at 584.32 cm^{-1}.

Morphological analysis via SEM further supports the observation that reduced crystallinity came with higher $[Li^+]_0$. As shown in **Figure S5c**, Li_3PO_4 pellets obtained at 1000 mg/L exhibit well defined, rod like structures with a relatively narrow size distribution. At 2500 mg/L (**Figure S5d**), Li_3PO_4 crystals became increasingly agglomerated into densely packed clusters of fine particles, which is consistent with excessive nucleation rates and limited crystal maturation under high supersaturation conditions. EDS elemental mapping (**Figure S5e**) revealed the dominant presence of phosphorus (67.71%) and oxygen (32.29%) in the precipitate. Although lithium could not be detected due to its low atomic number and weak X-ray yield, the compositional ratio strongly supports the formation of Li_3PO_4.

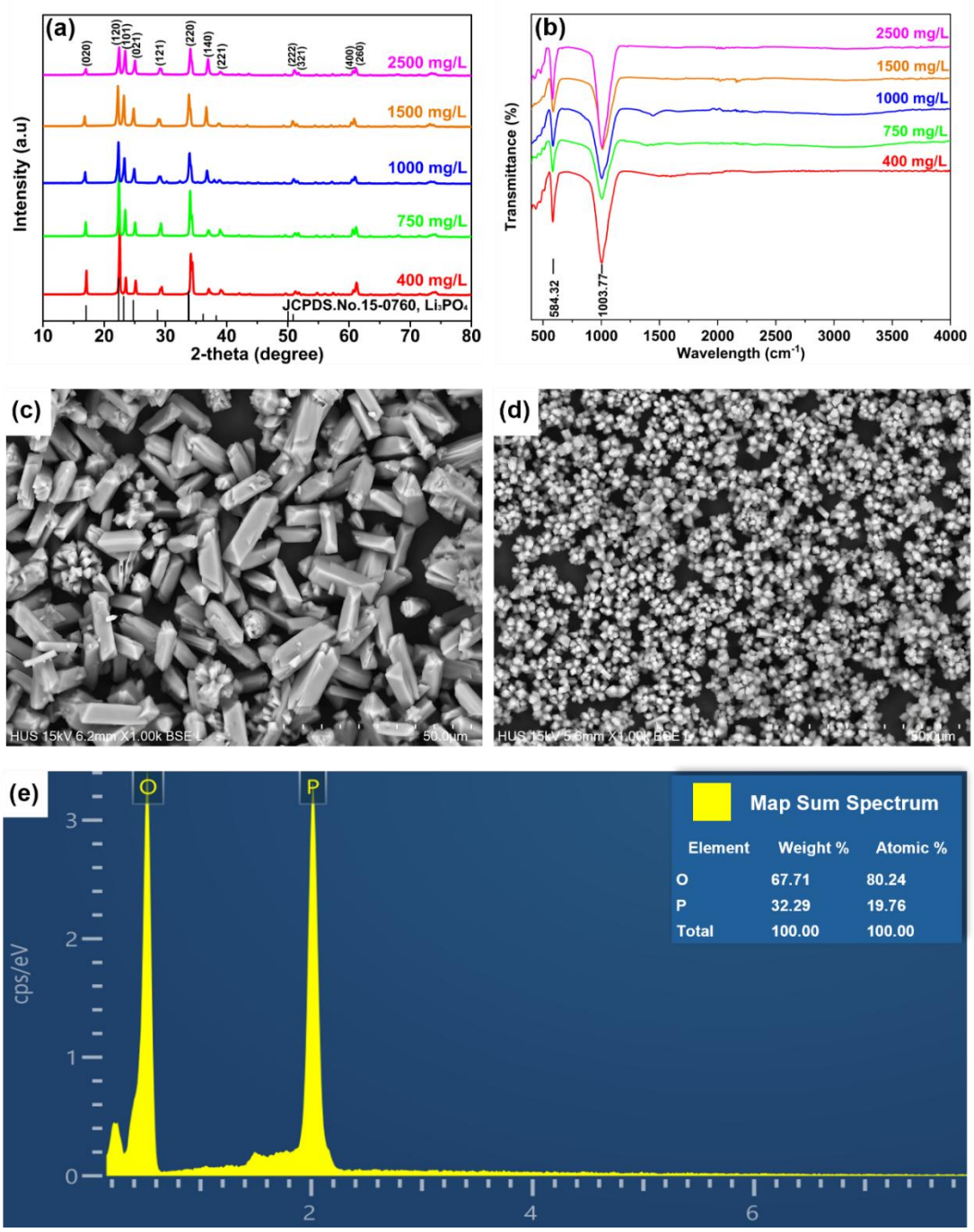

Figure S5. (a) XRD and (b) FTIR spectra of effects of different $[Li^+]_0$ on Li_3PO_4 pellets; SEM images of pellets at $[Li^+]_0$ (c) 1000 and (d) 2500 mg/L; (e) EDS mapping of pellets (experimental conditions: $[Li^+]_0$ of 1050 mg/L, pH_e of 11, L of 1 kg/m^2.h, T of 50 ^oC, $[PO_4^{3-}]_0/[Li^+]_0$ of 0.5, HRT ~200 h, and U of 15 m/h).

Text S6

XRD patterns of the product pellets at different effluent pH (pH_e)

Figure S6 displays XRD patterns of the product pellets obtained at different pH_e values under a $[PO_4^{3-}]_0/[Li^+]_0$ molar ratio of 0.5. Sharp characteristic peaks of lithium phosphate at 16.7°, 22.3°, 23.4°, 25.1°, 29.2°, 34.2°, 38.8°, 51.1°, and 63.3° for facets of (020), (120), (101), (021), (121), (220), (140), (222), and (260), respectively [3], (fitted with the standard of JCPDS. No. 15-0760), indicating the formation of crystalline Li_3PO_4. There is no obvious peak of the common side product Na_2HPO_4.

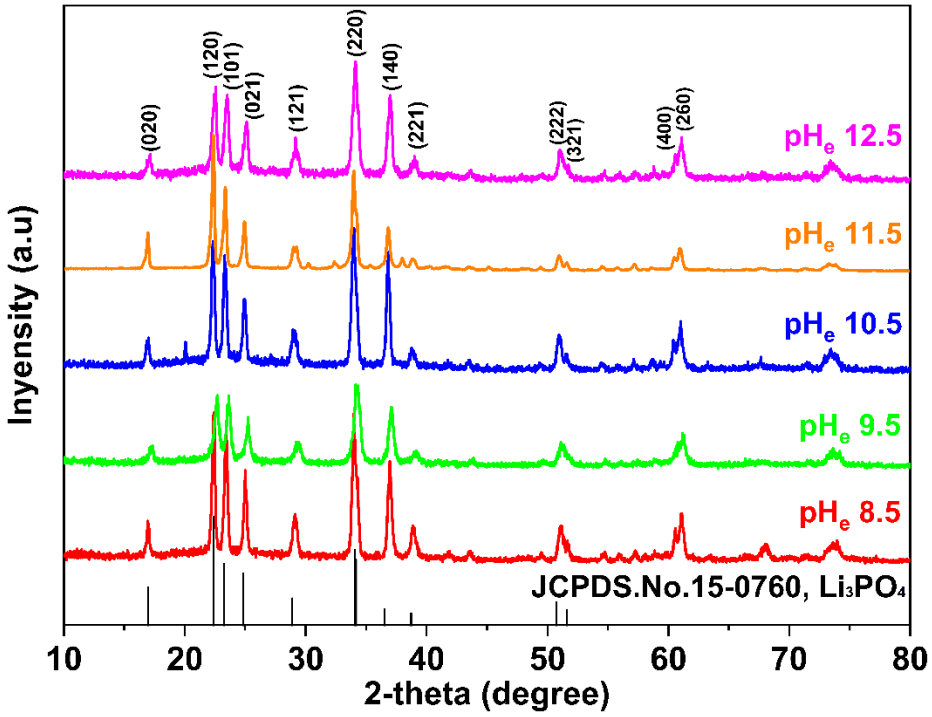

Figure S6. XRD spectra of effects of different pH_e on Li_3PO_4 pellets (experimental conditions: $[Li^+]_0$ of 1050 mg/L, L of 1 kg/m^2.h, T of 50 °C, $[PO_4^{3-}]_0/[Li^+]_0$ of 0.5, HRT ~200 h, and U of 15 m/h).

Text S7

Calculation of surface loading rates

It is essential to analyze the nucleation and growth that ensues in the region of sudden expansion inside the FBHC. Supersaturation conditions are defined by the hydrodynamic parameters that control the surface loading rate (L). That denotes the rate of the pollutant flow through the cross-sectional area of the lower column of the FBR.

$$L = \frac{Q_P \times [P]_{in}}{A} \qquad \text{(S6)}$$

Q_P is the influx flow rate (L/h) of the influent polluted wastewater (lithium or phosphate), $[P]_{in}$ the influent pollutant concentration (kg/L), and A is the cross-sectional area of lower column (3.14×10^{-4} m^2 for the reactor used).

Text S8

Kinetics of co-existing species in the FBHC process

$Li^+ + OH^- \leftrightarrow LiOH$ $K_1 = 10^{0.36}$ [S7]

$Li^+ + HPO_4^{2-} \leftrightarrow LiHPO_4^-$ $K_1 = 10^{-0.72}$ [S8]

$HPO_4^{2-} \leftrightarrow PO_4^{3-} + H^+$ $K_{sp3} = 10^{-12.35}$ [S9]

$H_2PO_4^- \leftrightarrow HPO_4^{2-} + H^+$ $K_{sp2} = 10^{-7.20}$ [S10]

$H_3PO_4 \leftrightarrow H_2PO_4^- + H^+$ $K_{sp1} = 10^{-2.04}$ [S11]

$H_2O \leftrightarrow OH^- + H^+$ $K_2 = 10^{-14}$ [S12]

$Li_3PO_{4(s)} \leftrightarrow 3Li^+ + PO_4^{3-}$ $K_{sp3} = 10^{-10.63}$ [S13]

$Li^+_{(aq)} + PO^{3-}_{4(aq)} \leftrightarrow LiPO^{2-}_{4(aq)}$ [S14]

$Li^+_{(aq)} + LiPO^{2-}_{4(aq)} \leftrightarrow Li_2PO^-_{4(aq)}$ [S15]

$Li^+_{(aq)} + Li_2PO^-_{4(aq)} \leftrightarrow Li_3PO_{4(aq)}$ [S16]

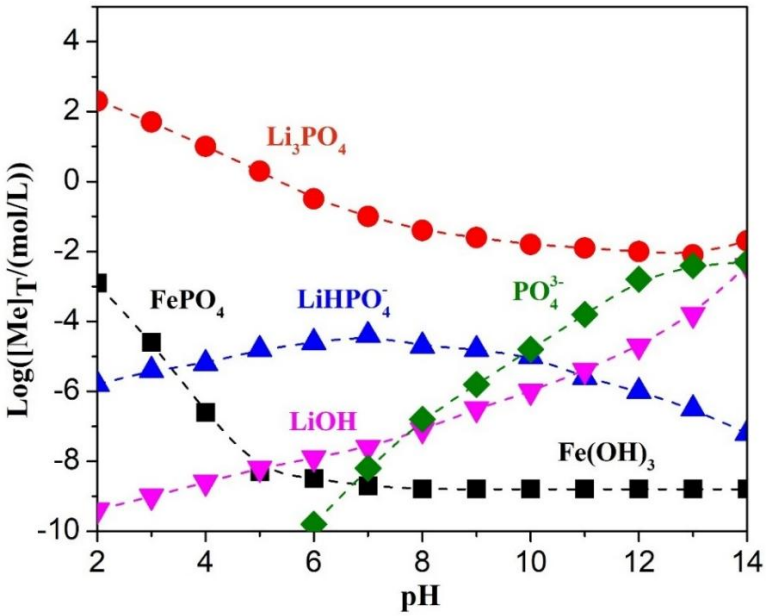

Figure S7. The Log[Me]T-pH diagram of species co-existing in the FBHC reactor.

Table S2. Elemental composition of Li_3PO_4 pellets

	wt.%
Li^+	16.0±2.8
PO_4^{3-}	26.6±5.4
Li_3PO_4	94.3±4.2

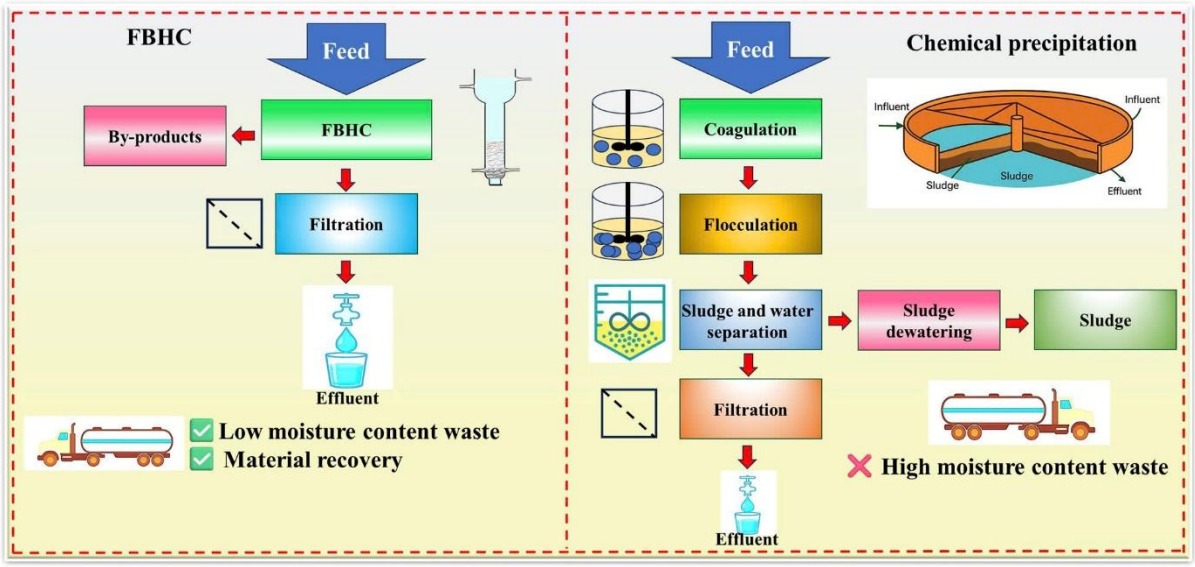

Figure S8. A process overview comparison between Fluidized Bed Homogeneous Crystallization (FBHC) and chemical precipitation.

Table S3. Comparative evaluation of lithium recovery technologies

	Feedstock type	Operating conditions	Recovery efficiency	Product purity	Product form	Scalability	Key limitations
Chemical precipitation	Synthetic Li^+ solution	T 90°C, pH 9.5, $[Li^+]$ 2 g/L, $[PO_4^3]/[Li^+]$ 1, 8 h batch	TR 95.4%	99.1% (Li_3PO_4)	Amorphous precipitate	Moderate	Sludge formation, Poor filterability, Batch operation.
Adsorption	Synthetic brine wastewater	0.05 g HMGO adsorbent, 2 h, pH 10, 180 rpm, 45 °C	Capacity 26 mg/g	Not applicable	Loaded adsorbent (no salt)	Low	Requires regeneration, Not a crystallization-based method.
Electrochemical precipitation	Li_2CO_3 leachate	T 90°C, $[PO_4^3]/[Li^+]$ 1, electrolysis setup	TR 88.46%	99.6% (Li_3PO_4)	Crystalline precipitate	Moderate	Energy-intensive, Requires electrodes/membranes.
Biofilm-coupled precipitation	Synthetic wastewater	T 80°C, $[Li^+]$ 2 g/L, pH 8.5, 8 h batch	TR 93.5%	Li_2CO_3	Biogenic precipitate	Low–Moderate	Complex biological control, Long residence time.
Solvent extraction	Synthetic solution	D2EHPA + kerosene, T 25°C, pH 4, shaking extraction, stripping by Na_2CO_3	TR 99.72%	99.9% (Li_2CO_3)	Solution-phase product	Low	Use of hazardous solvents, Multi-step separation.

Ultrasound-assisted precipitation	Synthetic solution	T 333 K, 35 min, ultrasound power 150 W, pH 10	TR 85.1%	95.5% (Li_3PO_4)	Fine precipitate	Low	Requires ultrasound equipment, Scale-up challenges.
Stripping + crystallization	Li^+-rich organic phase	0.3 M H_3PO_4, kerosene medium, batch operation, pH 8.2	TR 92.2%	92.2% (Li_3PO_4)	Mixed crystals	Moderate	Volatile solvents, Phase transfer sensitivity.
Homogeneous–heterogeneous precipitation	Synthetic solution	T 40°C, $[PO_4^3]/[Li^+]$ 1, pH 9, 300 rpm	TR 70%	80%	Mixed-phase precipitate	Low	Poor phase selectivity, Low recovery and purity
FBHC (This Study)	Real industrial wastewater	Continuous flow, T ambient, pH 8–11.5, $[Li^+]$ 710 mg/L, $[PO_4^3]/[Li^+]$ 0.5	TR ~92%, GR ~90%	~98% (Li_3PO_4 granules)	Granular crystalline product	High	Sensitive to co-ions (e.g., Na^+, Ca^{2+}), Optimization of hydrodynamics is still needed

REFERENCES

[1] K.C. Nnakwo, F.E. Amadi, V.S. Aigbodion, J.N. Ezeanyanwu, C.C. Nwogbu, A.O. Agbo, E.N. Okigbo, C.C. Daniel-Mkpume, Improving the thermo-physical behavior of Li2O-Al2O3-P2O5-SiO2 glass–ceramic system by triple-step heat treatment processes, The International Journal of Advanced Manufacturing Technology, 129 (2023) 3447-3452.

[2] X. Liu, X. Shen, H. Li, P. Li, L. Luo, H. Fan, X. Feng, W. Chen, X. Ai, H. Yang, Ethylene carbonate-free propylene carbonate-based electrolytes with excellent electrochemical compatibility for Li-ion batteries through engineering electrolyte solvation structure, Advanced Energy Materials, 11 (2021) 2003905.

[3] T. Ohnishi, K. Takada, Sputter-deposited amorphous Li3PO4 solid electrolyte films, ACS omega, 7 (2022) 21199-21206.